Extensive hydrated silica materials in western Hellas Basin, Mars

Joshua L. Bandfield, Elena S. Amador, Nancy H. Thomas

Earth and Space Sciences, University of Washington, Seattle, WA 98195-1310

Manuscript Correspondence:
Joshua Bandfield
Earth and Space Sciences
University of Washington
Seattle, WA 98195-1310
joshband@u.washington.edu
206-685-1910

Manuscript Pages: 27
Figures: 8

Abstract

Near-infrared spectral data indicate the presence of hydrated, poorly crystalline silica where high bulk silica contents have been previously identified in Hellas Basin. No other aqueous phases are identified in these regions and the deposits may be nearly pure. The silica-bearing surfaces are sporadically exposed along a 650 km stretch of the western basin rim within a limited elevation range and display a variety of surface textures suggesting that the materials have been reworked, but not transported large distances. The high abundances and lack of associated aqueous phases indicate that high water to rock ratios were present in the region during the Noachian period but without elevated temperatures or for durations necessary for quartz diagenesis. The silica-bearing materials may have formed via direct precipitation from silica saturated groundwater sources, although other formation mechanisms are also plausible.

Highlights

- Hydrated silica and bulk high silica materials have been identified in Hellas Basin
- The high silica deposits may be nearly pure and no other phases have been detected
- The exposures cover an extensive region but are restricted in elevation
- Large amounts of water were required for their formation, but with limited diagenesis

1. Introduction

A large diversity of martian aqueous compositions have been identified via orbital and in situ observations, revealing a planet with a variety of alteration processes that have been present throughout martian history. The presence of phyllosilicates alone reveals evidence of a diversity of alteration environments based on the detection of smectite, kaolinite, and illite group minerals (e.g., *Poulet et al.*, 2005; *Bishop et al.*, 2008; *Mustard et al.*, 2009). Similar clues that build a more coherent understanding of past aqueous environments can be elucidated from the detailed investigation of other compositions such as chlorides (*Osterloo et al.*, 2008), sulfates (e.g., *Gendrin et al.*, 2005), hematite (*Christensen et al.*, 2001a), carbonates (*Bandfield et al.*, 2003; *Boynton et al.*, 2009; *Ehlmann et al.*, 2008), and silica (e.g., *Miliken et al.*, 2008; *Ruff et al.*, 2011). Not only do these compositions indicate the presence of liquid water in past martian environments, their compositional and geomorphological associations have been used to more specifically define the aqueous environment present at the time of formation (e.g., *Mustard et al.*, 2009).

Previous work by *Bandfield* (2008) identified high silica phases exposed in western Hellas Basin near 48°E, 42°S using Mars Global Surveyor Thermal Emission Spectrometer (TES; *Christensen et al.*, 2001b) and 2001 Mars Odyssey Thermal Emission Imaging System (THEMIS; *Christensen et al.*, 2003) data. Analysis of these data indicates the presence of surfaces composed of nearly 80 areal % high silica phases. This is significantly higher than other regions containing high silica bulk compositions identified from orbit (*Bandfield et al.*, 2000; *Bandfield et al.*, 2004a; *Christensen et al.*, 2005) and is similar to the 90% silica abundance compositions identified near the Home Plate feature in the Columbia Hills of Gusev Crater

(*Squyres et al.*, 2008; *Ruff et al.*, 2011).

The high silica surfaces themselves are coincident with mantled and layered terrains that show evidence of deformation and flow and the high silica materials may have been transported from their original formation location. Though the layered and mantled terrains may have an influence on the formation of the high silica surfaces, *Bandfield* (2008) noted that this terrain is extensive throughout the Hellas Basin region, whereas the high silica deposits are not.

The specific phases present in Hellas Basin are ambiguous based on analysis of the thermal infrared data alone and were interpreted by *Bandfield* (2008) as some combination of poorly crystalline to amorphous silica, phyllosilicates, and/or zeolites. The high silica deposit spectral signature was derived from only a fraction of a single TES spectral measurement and did not have the necessary signal to noise ratio to confidently exclude the presence of any of these phases. In addition, it was suggested by *Bandfield* (2008) that sulfates may be present, though the limited spatial extent of the deposits also prevented a confident identification.

The western Hellas Basin high silica deposits are only one of a variety of exposures planet-wide (*Smith et al.*, 2013). Hydrated and poorly crystalline phases of silica appear to be one of the most commonly identified alteration product on Mars, which formed in a variety of environments (*Ehlmann et al.,* 2009; *Glotch et al.*, 2006; *Marzo et al.*, 2010; *Wray et al.*, 2011; *Weitz et al.*, 2011; *Milliken et al.*, 2008; *Squyres et al.* 2008; *Skok et al.* 2010; *Rice et al.*, 2010; *Ruff et al.,* 2011; *Smith and Bandfield,* 2012). Despite the general compositional similarity, there are distinct morphological and specific mineralogical differences that make these surfaces unique relative to one another. Detailed characterization and comparison can be used to better understand the variety of aqueous environments present and the extent and duration of exposure

to water (e.g., *Tosca and Knoll*, 2009; *Smith et al.*, 2013).

With the addition of greater spatial coverage, near-infrared spectral data, and high spatial resolution images, we have been able to more fully characterize the composition, extent, and geological context of these unique surfaces. Specifically, we have identified hydrated silica-bearing materials using data acquired by the Compact Reconnaissance Imaging Spectrometer for Mars (CRISM; *Murchie et al*., 2007). Although CRISM has a higher native spatial resolution than THEMIS (18 m versus 100 m), most additional detections described here were identified using the 200 m/pixel multispectral survey data products. The new detections here are primarily due to the additional spatial coverage and the added confidence in detections using both near- and thermal-infrared wavelength regions. No other aqueous phases are detected and the combined use of near-infrared and thermal infrared wavelength regions with complementary sensitivities has been used to better constrain the surface mineralogical properties. These deposits are also found to be much more extensive than previously identified by *Bandfield* (2008).

2. Data and Methods

2.1 THEMIS Data

The THEMIS thermal infrared imager consists of a 320 by 240 element uncooled microbolometer array with 9 spectral channels centered at wavelengths between ~7 and 15 μm and a spatial sampling of 100 m. More detailed descriptions of calibration methods and radiometric uncertainties are presented in *Christensen et al.* (2004) and *Bandfield et al.* (2004b). All data used in the analyses presented here were acquired at afternoon local times of

~1400-1800 at near-nadir observation geometries.

We used multispectral thermal infrared THEMIS images to identify surfaces with a high bulk SiO_2 content. These high silica deposits are distinguished from other surface compositions using THEMIS bands 6, 4, and 2 (centered near 9.66, 7.98, and 6.27 μm) projected as red, green, and blue respectively in decorrelation stretch (DCS) images. The DCS images can be used to rapidly identify spectrally unique surfaces using calibrated radiance data (*Gillespie et al.*, 1986) without the need for the extensive processing typically required for producing atmospherically corrected surface emissivity. The high silica surfaces have low emissivity values at wavelengths corresponding to THEMIS band 4 within the ~8-12 μm Si-O Restrahlen band, resulting in a distinct magenta color in the DCS images (Figure 1). By contrast, basaltic and dusty surfaces have low emissivity values in THEMIS bands 6 and 2 respectively, resulting in cyan and yellow/green colors in the THEMIS DCS images. All warm (average 12 μm brightness temperature, which approximates surface kinetic temperature, greater than220K) THEMIS images (up to orbit 44000) were inspected for the presence of high silica deposits within Hellas Basin.

No additional thermal infrared spectral information was found to be present in the newly identified high silica exposures described here. Consequently, THEMIS data was used only to locate new exposures of the high silica units and we rely here on the spectral analysis of *Bandfield* (2008) for compositional interpretation of the thermal infrared data using the TES and THEMIS data.

2.2 CRISM Data

The CRISM) is a scanning imaging spectrometer covering 0.362-3.92 μm wavelengths with

0.00655 μm sampling. Data are collected at several spatial resolutions and spectral sampling modes. For this work, we used full- and half-resolution targeted (FRT, HRL, HRS) near-infrared (~1.0-3.9 μm) I/F data products, which include full spectral coverage at ~18 or 36 m/pixel sampling. We also used multispectral survey products (MSP), which sample 55 wavelengths between ~1.0 and 3.5 μm at 200 m/pixel sampling. The reduced spatial resolution and spectral coverage of MSP products allow for greater spatial coverage within the data bandwidth constraints of the Mars Reconnaissance Orbiter (MRO) spacecraft. CRISM data with excessive noise or collected during periods of high water-ice opacities in Hellas Basin were excluded from the analysis, limiting the spatial coverage (Figure 2; Table 1). All data were corrected for atmospheric gas absorptions using the volcano scan method as described by *McGuire et al.* (2009) and only TRR3 data products were used, which include improved noise reduction algorithms relative to previous versions.

Spectral index images were produced from the CRISM data in a manner similar to that described by *Pelkey et al.* (2007), but additional indices were included for the identification of specific phases, such as hydrated silica and carbonates. In particular, we relied heavily on a spectral ratio index (2.14 / 2.25 μm; the average of CRISM full spectral resolution samples 262 through 271 divided by the average of samples 243 through 257; for multispectral data we used CRISM samples 26 through 27 and 22 through 24) to identify the Si-OH absorption feature near 2.25 μm (*Rice et al.*, 2013). This feature is a combination of overlapping absorptions near 2.21 and 2.26 μm that have variable relative strengths contributing to an asymmetrical appearance. For the surfaces presented here, this leads to an appearance of a band minimum near 2.25 μm, hence the label we attribute to the feature here. Regardless, the index incorporates a range of

wavelengths spanning ~2.19-2.29 μm, making it sensitive to the magnitude rather than the asymmetry of the absorption.

We used a simple ratio rather than a band depth index to avoid noise and other interfering factors due to the inclusion of additional spectral bands. This noise is especially prevalent in the multispectral data and interpretation of the spectral index images was significantly easier using a simple ratio index. Although values returned by a simple ratio can be influenced by spectral slopes that are unrelated to band depth, this was not the case for the data shown here.

Index images were produced using a standard deviation stretch to show the relative variation within a scene. Values were assigned a rainbow color scale and draped over corresponding Context Camera (CTX; Malin et al., 2007) images to show the associated high spatial resolution morphology. Each image was stretched uniquely to draw attention to local variations in the index values, but preventing quantitative comparison of index values between images. This is necessary because of the highly variable atmospheric conditions present near Hellas Basin throughout the martian year that make it impossible to directly compare images without the application of more rigorous atmospheric compensation methods. In addition, CRISM data are acquired under a variety of viewing geometries, further complicating comparison between images uncorrected for atmospheric aerosols.

Where the indices displayed spatial variation for a particular phase of interest, individual I/F spectra were inspected. Although the index appears to be relatively uniquely triggered by the presence of hydrated silica, it is necessary to manually inspect plotted spectra from a high index value surface. This ensures that high index values are not being triggered by environmental effects or the presence of other surface compositions that would lead to false identifications. To

cancel residual noise and atmospheric effects, spectral ratios were produced using a nearby surface as the denominator. Although no surface on Mars is spectrally neutral and spectral ratios can be a complex mixture of positive and negative absorption features, in practice this is an effective method for the identification of narrow and prominent absorptions, such as those present in many hydrated phases and carbonates at near-infrared wavelengths (e.g., *Poulet et al.*, 2005; *Murchie et al.*, 2007; *Milliken et al.*, 2008; *Ehlmann et al.*, 2008; *Bishop et al.*, 2008; *Smith and Bandfield*, 2012).

Although spectral indices can provide a quantitative assessment, they are subject to interference from systematic noise and variable atmospheric conditions and viewing geometries. We initially relied solely on parameters such as the 2.25 μm band ratio index images, but found that this resulted in many false detections and missed identifications that were verified using separate observations covering the same surfaces. Consequently, we rely on visual identification of spectral absorptions for the presence of any particular phase, which can be subjective. Our methodology only identified instances where the spectral shape is clearly defined (meaning the presence of clearly identifiable 1.9 and 2.25 μm absorption features in the case of hydrated silica) to ensure only potential errors of omission in our results. Finally, the definition of spatial boundaries for these units are subject to similar subjective criteria, but in most cases, surface compositional unit boundaries are well-defined over hundreds of meters to kilometer scales.

2.3 Other Datasets

In addition to the spectral datasets, we used data from the High Resolution Imaging Science Experiment (HiRISE; *McEwen et al.*, 2007) and CTX on-board MRO to characterize surface textures and morphology. Where available, HiRISE images (sampled at ~0.25-0.5 m/pixel) were

used to identify fine-scale surface textures and features such as individual boulders. However, we more typically relied on CTX images (sampled at ~5.5 m/pixel) for surface morphological and textural information because of the much more extensive spatial coverage of this dataset.

Other datasets used in this study include gridded Mars Orbiter Laser Altimeter (*Smith et al.*, 2001) data used to characterize deposit elevations, and THEMIS nighttime thermal infrared images. The nighttime THEMIS data were used to characterize surface thermophysical properties. We did not calculate thermal inertia values from the THEMIS data (*Fergason et al.*, 2006), but simply used the nighttime radiance images to identify thermophysically distinct surface units.

3. Results

3.1 Hydrated Silica Distributions

Index images derived from CRISM data in western Hellas Basin (image ID's are provided in supplemental data) display coherent spatial concentrations consistent with elevated absorption band depths near 1.9 and 2.25 μm (Figure 3). Although spatial coverage of high quality CRISM data is incomplete, the data show numerous exposures consistent with the presence of hydrated silica in the same region where high silica compositions were identified using thermal infrared datasets (*Bandfield*, 2008; Figure 1). The index images shown in Figure 3 show distinct regions of elevated hydrated silica index values and each distinct region (excluding obvious data artifacts, such as along-track striping) that appears orange/red in Figure 3 was checked using spectral ratios to confirm the presence of distinct 1.9 and 2.25 μm absorptions.

In most cases, the hydrated silica-bearing surfaces correspond with locations that we interpret

to be dominated by high silica phases based on our analysis of the thermal infrared spectral data. However, there are additional surfaces that also indicate the presence of hydrated phases not apparent in thermal infrared observations (Figure 4). In some of these cases, the surface is colder in nighttime THEMIS data. This indicates the presence of a lower thermal inertia surface dominated by fine particulates that contribute to a reduced spectral contrast, preventing detection using the THEMIS data. In other cases, surface temperatures are low in the daytime THEMIS data (≤230K), reducing the signal to noise ratio and preventing detection in THEMIS DCS images (*Bandfield et al.*, 2004b).

CRISM index images also indicate the presence of high calcium pyroxene (using the HCP index described by *Pelkey et al.*, 2007) coincident with low albedo materials present in the region (Figure 5). This is consistent with the presence of basaltic materials identified using the thermal infrared data (*Bandfield*, 2008). No sulfate, phyllosilicate, or carbonate phases were identified using CRISM index images or spectral ratios.

All exposures of hydrated silica occur on the western and northwest interior of Hellas Basin are and are much more extensive than previously identified (Figure 2). Exposures span a distance of ~650 km from 33.6°S to 43.8°S (Table 2). Most exposures are confined to 37.1°S to 43.8°S and all are restricted to elevations between -6500 to -5000 m. A relatively isolated exposure of hydrated silica occurs near 53.1°E, -33.6°S, about 280 km northeast of the main cluster of hydrated, high silica deposits. Based on analysis of CRISM index images, individual exposure areal coverage ranges from <1 to 59 km^2 and the total area of hydrated silica exposures is 449 km^2. These values were determined by a qualitative assessment of the index images as described in the Methods and Data section and are only approximate. Actual coverage is likely

to be significantly greater because CRISM data coverage is incomplete. Despite the incomplete coverage, the regional extent of the hydrated silica materials is likely to be well characterized because there are numerous exposures and Hellas Basin is well-sampled by CRISM data without extended regional gaps in coverage.

3.2 CRISM Spectral Analysis

CRISM I/F spectral ratios display clear evidence for the presence of hydrated phases with absorptions present near 1.4, 1.9, and 2.25 μm (Figures 6 and 7; Table 3), consistent with the presence of hydrated silica. The 1.4 μm band is due to an OH^- vibrational overtone, an H_2O overtone causes the absorption near 1.9 μm, and SiOH vibrational overtones cause the absorptions near 2.25 μm. The 1.4 and 1.9 μm features are often weak and difficult to distinguish from other hydrated phases. Consequently, detections of silica here are based primarily on the presence of a 2.25 μm absorption. The spectral ratios were used to validate the compositional interpretations using the index images discussed above. The spectra bear similarities to other martian regions where hydrated silica has been identified, such as Valles Marineris (*Milliken et al.*, 2008), Syrtis Major (*Ehlmann et al.*, 2009), and Noctis Labyrinthus (*Weitz et al.*, 2011; Figure 7). Although variations are present in the specific shape and strength of the absorptions between the different locations (*Smith et al.*, 2013), it is difficult to uniquely identify a specific phase (e.g. opal-A versus opal-CT) from the spectral data (*Rice et al.*, 2013). *Smith et al.* (2013) and *Rice et al.* (2013) describe the formation processes and resulting spectra of various hydrated silica phases in detail.

Despite this difficulty, the crystallinity of hydrated silica shows systematic trends with the precise wavelength of the 1.4 μm absorption and the ratio of the 1.91 to 1.96 μm absorption band

depths (*Rice et al.*, 2013; *Smith et al.*, 2013). The CRISM multispectral data (accounting for the majority of hydrated silica detections in the region) do not have the spectral resolution to allow for the precise determination of the absorption band centers, but this analysis can be applied to a single full spectral resolution CRISM image within the region where these absorption features are well-defined. The hydrated silica exposures identified in CRISM image HRL00013366 have an absorption center at 1.415 μm and a 1.91/1.96 band depth ratio of 1.064 (*Smith et al.*, 2013). These values are similar to those of hydrated silica exposures identified in Noctis Labyrinthus, Isidis Basin, and Toro Crater and are consistent with intermediate hydrated silica phases with limited short order crystalline structure such as opal-A, rather than hydrated glass or microcrystalline quartz (*Smith et al.*, 2013). Variations in the shape of the 2.25 μm absorption appear to be present within the region (Figure 6), but it is not clear if we can attribute these variations to the surface composition or other factors that may affect the multispectral CRISM data.

3.3 Associated Morphologies and Thermophysical Properties

Exposures of the hydrated, high silica materials typically occur in local topographic lows and are not present within high standing knobs or ridges. Dark toned dust devil tracks and basaltic sand dunes are commonly adjacent to the silica exposures and both dust devils and saltating sand provide a means to clean surfaces of mantling dust and expose the deposits. Although often adjacent to dunes, the silica bearing deposits do not appear coincident with the dunes themselves (Figures 5 and 8). In other locations, the silica-bearing surfaces are adjacent to layered materials that in some cases appear to have been deformed or display indications of viscous flow (*Bandfield*, 2008). The exposures are often diffuse without clear morphological boundaries, but

there are also instances where a topographic step defines a boundary between silica-poor and hydrated silica units (Figure 8b).

The silica-bearing deposits display a variety of surface textures (Figure 8). These textures include a smooth mantling unit that appears to have surface collapses near its periphery due to a volume removal process such as dessication (Figure 8c). Other silica-bearing surfaces are dominated by a uniform field of ripple forms with meter scale wavelengths (Figure 8f). A third surface texture associated with these compositions is smooth with periodic sub-meter scale knobs (Figure 8d). In addition, silica-bearing units are present that cross these morphological boundaries (Figure 8e).

Nighttime THEMIS temperature images indicate that these materials span a variety of thermophysical units suggesting that the silica-bearing materials also span a range of particle sizes and/or degree of consolidation (Figure 9). In general, however, the hydrated silica exposures are correlated with surfaces that have relatively low nighttime temperatures. For example, dune forms adjacent to hydrated silica exposures have warmer nighttime temperatures, indicating that dunes have a greater degree of consolidation and/or larger particle sizes than the hydrated silica deposits. In one instance (near 47.75°E, 43.73°S), hydrated silica bearing deposits are coincident with surfaces that have relatively low nighttime temperatures, indicating that the surface consists of more poorly consolidated or finer particulates than the surrounding terrain. This particular hydrated silica exposure lacks a positive detection of high silica compositions in the thermal infrared data. This is consistent with the presence of a lower thermal inertia material because fine particulates typically have significantly reduced thermal infrared spectral contrast that makes detection difficult where these fine particulate materials are present.

Regardless, the low nighttime temperatures of all surfaces relative to the dunes in the region indicates that surface exposures are loose or poorly consolidated and are not consistent with exposures of bedrock.

4. Discussion

4.1 Surface Mineralogy

The surfaces of interest here are dominated by high concentrations of hydrated, poorly crystalline silica phases. There is also a lack of sulfates, clays, and other hydrated phases detected using the near-infrared data and low quantities of quartz and plagioclase (along with a lack of igneous low-Si phases) detected using the thermal infrared data. The hydrated silica detected using the CRISM data is typically co-located with the high-Si abundance materials detected using the TES/THEMIS data. Where the thermal infrared and near-infrared datasets do not show this agreement, it is possibly due to measurement sensitivity limitations (data quality, particle sizes, and surface temperatures) rather than intrinsic differences in composition.

Based on analysis of the thermal infrared data alone, *Bandfield* (2008) determined that the high silica surfaces were dominated by an amorphous silica phase similar to hydrated glass or opaline silica. Other components, such as sulfates were also present in the deconvolution results, but could not be confidently identified due to the limited extent of the exposure and the relatively large footprint of the TES spectral measurements. In addition, because of the similarity between certain phyllosilicates, zeolites, and amorphous silica phases in the thermal infrared spectra (*Ruff and Christensen*, 2007), the specific high silica phase itself could have included large amounts of phyllosilicates and zeolites in addition to amorphous phases. The combined analysis of

near-infrared and thermal infrared spectroscopic datasets better constrains the composition and distribution of the deposits, which are also significantly more extensive than previously thought. Previous work identified high silica deposits within an isolated local area ~50 km across near 48.0°E, 41.5°S (*Bandfield*, 2008). The newly identified high silica surfaces span a region that is an order of magnitude larger (~650 km) from 33.6°S to 43.8°S (Table 2).

It is likely that dust cover and other mantling materials are likely hiding other occurrences. High silica surface exposures are typically located near dune deposits that are likely scouring nearby surfaces and keeping them relatively free of dust. The sand deposits are much more extensive and and common within the region than the high silica surfaces. This indicates that the high silica surfaces are probably restricted to the do not commonly occur outside the region in which they have been identified.

The inclusion of near-infrared spectral data to our analysis both confirms the results of *Bandfield* (2008) and adds significant detail that can be used to refine and constrain formation hypotheses. The CRISM data show no evidence for the presence of any additional phases, such as sulfates, phyllosilicates, or zeolites. Given the identification of high concentrations of amorphous silica and the lack of evidence for any additional phases in both the near-infrared and thermal infrared spectral data, the high silica deposits may be nearly pure. Based on spectral deconvolution analysis (e.g., *Ramsey and Christensen*, 1998), the high silica surfaces were determined to have ~80% high silica phases and the other 20% were identified as sulfates (below detection limits for the limited data; *Bandfield*, 2008). Sulfates and high silica phases can have absorptions in the thermal infrared at similar wavelengths and it is possible that they were erroneously substituted for additional high silica phases by the spectral deconvolution algorithm.

Despite these additional constraints, we caution against leaning too heavily on the non-detection of any particular phase for the interpretation of the surface composition. There is ample evidence for unequivocal identifications of mineral phases on Mars via one measurement technique where another technique shows no evidence for the same phase (*Bandfield et al.*, 2011). Particle sizes, surface textures, atmospheric conditions, and surface temperature and illumination conditions can all interfere with the spectroscopic detection of compositional phases. In addition, although sulfates have been detected in numerous locations on the martian surface using near-infrared spectral data (e.g., *Gendrin et al.*, 2005), they may not be detected if they are not hydrated because the presence of H_2O and OH^- vibrational overtones are responsible for prominent diagnostic absorptions in sulfate near-infrared spectra (e.g., *Sutter et al.*, 2007).

4.2 Formation Environments

The silica-bearing deposits discussed here are compositionally similar to those identified near Home Plate within Gusev Crater (*Squyres et al.*, 2008; *Ruff et al.*, 2011). Nearby sulfate bearing deposits and evidence of local hydrovolcanic activity led *Squyres et al.* (2008) to conclude that the silica bearing deposits in Gusev Crater likely formed by acid leaching. However, based on more detailed compositional and textural analyses, *Ruff et al.* (2011) favor a precipitation formation mechanism, specifically under hydrothermal conditions.

Hydrated and poorly crystalline silica form in a variety of environments (for more complete discussions see *Ruff et al.*, 2011 and *Smith et al.*, 2013). For example, acid leaching can dissolve and transport away more soluble materials leaving behind high concentrations of amorphous silica, which is relatively insoluble under low pH conditions. By contrast, under both hydrothermal and low temperature conditions, silica saturated water commonly directly

precipitates opaline silica. In similar, but relatively water-limited environments, minor amounts of water can break down minerals and re-precipitate thin coatings of amorphous silica on rock surfaces.

If the spectroscopic analyses presented here are taken at face value, the silica-rich surfaces in Hellas Basin are dominated by a hydrated amorphous silica phase with no other detectable components. There is no evidence for a nearby source of acidic waters and we found no other commonly associated minerals (e.g., sulfates) within the restricted elevation range. An extensive source of acidic groundwater is also unlikely since it would be quickly neutralized as it permeates through the basaltic crust. Based on these observations, acid leaching is not our favored hypothesis for the formation of the high silica surfaces. However, we cannot completely rule out acid leaching because these arguments are largely based on a lack of direct evidence rather than any clear contradicting observation.

We believe that silica coatings are also an unlikely explanation for the high silica surfaces due to the extensive nature of the deposits and high concentrations of silica phases. The presence of thin silica coatings would require ubiquitously coating all grains of reworked sediments rather than simply exposing regolith or rock surfaces in their original formation environment. Despite this, it is possible that silica precipitated on grain surfaces in the subsurface, producing a substantial volume of coated particles. This is, after a manner, similar to the direct precipitation mechanism discussed below.

We favor a direct precipitation mechanism for the genesis of the high silica deposits in Hellas Basin. Under these conditions, relatively large amounts of water are required to dissolve and re-precipitate high concentrations of high silica phases across the western rim of Hellas Basin.

There is no evidence for diagenesis, which indicates a limited duration of exposure to water, especially under elevated temperature conditions (*Tosca and Knoll*, 2009). The presence of quartz would provide the clearest evidence for diagenesis. Despite the presence of the highest concentrations of high silica phases identified from orbit, there is no evidence for crystalline quartz in TES data. However, TES measurements are only capable of resolving the largest exposures of the high-Si deposits and neither the current TIR or NIR datasets have the capability to evaluate variations in crystallinity across the region. The lack of diagenesis is similar to other hydrated silica deposits identified on Mars that also have limited crystallinity, with the exception of quartz identified in the Syrtis Major/Antoniadi Crater region (*Smith et al.*, 2013; *Smith and Bandfield*, 2012).

4.3 Geologic Context

The association of the silica-bearing deposits with local topographic lows and a variety of surface textures and morphologies, including ripple forms and mantling units indicates that this material has been mobilized and reworked. Detailed geomorphic mapping of the region (*Moore and Wilhelms*, 2007) also indicates that the silica-bearing deposits cover a variety of surface units with ages ranging from the late Noachian to Amazonian Eras. This region has been interpreted as being dominated by sediments from a past lake filling much of Hellas Basin.

The relatively limited extent of the silica-bearing deposits compared to the sedimentary units suggests that the influence by a lake present in Hellas Basin may have been restricted to mechanical reworking of preexisting Noachian silica-bearing materials within the region. The presence of hydrated, high silica materials within layered and deformed surface units also suggests that the silica-bearing materials have been reworked under periglacial processes

associated with recent climate cycles. That these materials are not in-place prevents their detailed morphological and textural analysis of the original formation environment. However, the confinement within a relatively narrow elevation range along the western edge of Hellas Basin indicates that the total distance material has been transported is probably limited.

The reworking of the high silica deposits makes it difficult to identify the specific geological context of their formation. The topographic gradient of the western edge of the basin may have intersected the local groundwater table and permeable lithologies, allowing for the formation of springs and precipitation of silica with exposure to the martian surface environment. Although there is no clear evidence for fluvial activity in the immediate vicinity of the deposits, it may have been covered and modified by the pervasive mantling sedimentary units. There is ample evidence for fluvial dissection to the west (at elevations higher than the high-Si exposures) where the closest unmantled surfaces are exposed. In addition, the presence of such high concentrations of sedimentary silica implies the presence of its silica-poor complement. A groundwater source could leave the altered source materials buried where they would not be detected and provide a means to transport the silica to the surface. We acknowledge that other formation mechanisms are possible and present this scenario only as an initial hypothesis.

5. Conclusions

Hydrated, poorly crystalline silica is a common aqueous phase on Mars and its occurrence along the western rim of Hellas Basin appears to record one of a variety of formation environments on the planet. The high concentrations of silica present on the surface require relatively large amounts of water for their formation but the temporal extent of contact with water at high temperatures was likely limited based on the lack of diagenetic quartz. Although

subsequent reworking of the deposits has erased any associated morphological evidence, the exposure discussed here records what was likely an extensive source of water in western Hellas Basin early in martian history.

Acknowledgements

We would like to thank the Mars Odyssey and MRO operations teams for targeting, collecting, and archiving the various datasets used here. JMARS software was used for analysis of the multiple datasets. Melissa Rice and Christina Viviano provided helpful and thorough reviews that significantly improved and clarified the manuscript. Funding for this project has been provided in part by NASA MDAP grant NNX10AQ33G.

References

Bandfield, J. L. (2008) High-silica deposits of an aqueous origin in western Hellas Basin, Mars. *Geophys. Res. Lett*, *35*, 1220510.1029/2008GL033807.

Bandfield, J. L., A. D. Rogers, and C. S. Edwards (2011) The role of aqueous alteration in the formation of martian soils. *Icarus*, *211*, 10.1016/j.icarus.2010.08.028.

Bandfield, J. L., V. E. Hamilton, P. R. Christensen, and H. Y. McSween (2004a) Identification of quartzofeldspathic materials on Mars. *J. Geophys. Res.*, *109*, 1000910.1029/2004JE002290.

Bandfield, J. L., D. Rogers, M. D. Smith, and P. R. Christensen (2004b) Atmospheric correction and surface spectral unit mapping using Thermal Emission Imaging System data. *J. Geophys. Res.*, *109*, 1000810.1029/2004JE002289.

Bandfield, J. L., T. D. Glotch, and P. R. Christensen (2003) Spectroscopic Identification of Carbonate Minerals in the Martian Dust. *Science*, *301*, 1084-1087 10.1126/science.1088054.

Bandfield, J. L., V. E. Hamilton, and P. R. Christensen (2000) A Global View of Martian Surface Compositions from MGS-TES. *Science*, *287*, 1626-1630 10.1126/science.287.5458.1626.

Bishop, J. L., and 11 colleagues (2008) Phyllosilicate Diversity and Past Aqueous Activity Revealed at Mawrth Vallis, Mars. *Science*, *321*, 83010.1126/science.1159699.

Boynton, W. V., and 13 colleagues (2009) Evidence for Calcium Carbonate at the Mars Phoenix Landing Site. *Science*, *325*, 6110.1126/science.1172768.

Christensen, P. R., and 11 colleagues (2005) Evidence for magmatic evolution and diversity on Mars from infrared observations. *Nature*, *436*, 504-509 10.1038/nature03639.

Christensen, P. R., and 10 colleagues (2004) The Thermal Emission Imaging System (THEMIS) for the Mars 2001 Odyssey Mission. *Space Sci. Rev.*, *110*, 85-130 10.1023/B:SPAC.0000021008.16305.94.

Christensen, P. R., and 21 colleagues (2003) Morphology and Composition of the Surface of Mars: Mars Odyssey THEMIS Results. *Science*, *300*, 2056-2061 10.1126/science.1080885.

Christensen, P. R., R. V. Morris, M. D. Lane, J. L. Bandfield, and M. C. Malin (2001a) Global mapping of Martian hematite mineral deposits: Remnants of water-driven processes on early Mars. *J. Geophys. Res.*, *106*, 23873-23886 10.1029/2000JE001415.

Christensen, P. R., and 25 colleagues (2001b) Mars Global Surveyor Thermal Emission Spectrometer experiment: Investigation description and surface science results. *J. Geophys. Res.*, *106*, 23823-23872, 10.1029/2000JE001370.

Edwards, C. S., K. J. Nowicki, P. R. Christensen, J. Hill, N. Gorelick, and K. Murray (2011) Mosaicking of global planetary image datasets: 1. Techniques and data processing for Thermal Emission Imaging System (THEMIS) multi-spectral data. *J. Geophys. Res.*, *116*, 1000810.1029/2010JE003755.

Ehlmann, B. L., and 11 colleagues (2009) Identification of hydrated silicate minerals on Mars using MRO-CRISM: Geologic context near Nili Fossae and implications for aqueous

alteration. *J. Geophys. Res.*, *114*, 010.1029/2009JE003339.

Ehlmann, B. L., and 13 colleagues (2008) Orbital Identification of Carbonate-Bearing Rocks on Mars. *Science*, *322*, 182810.1126/science.1164759.

Fergason, R. L., P. R. Christensen, and H. H. Kieffer (2006) High-resolution thermal inertia derived from the Thermal Emission Imaging System (THEMIS): Thermal model and applications. *J. Geophys. Res.*, *111*, 1200410.1029/2006JE002735.

Gendrin, A., and 10 colleagues (2005) Sulfates in Martian Layered Terrains: The OMEGA/Mars Express View. *Science*, *307*, 1587-1591 10.1126/science.1109087.

Gillespie, A. R., A. B. Kahle, and R. E. Walker (1986) Color enhancement of highly correlated images: I. Decorrelation and HIS contrast stretches, *Remote Sens. Environ.*, *20*, 209– 235.

Malin, M. C., and 13 colleagues (2007) Context Camera Investigation on board the Mars Reconnaissance Orbiter. *J. Geophys. Res.*, *112*, 510.1029/2006JE002808.

McEwen, A. S., and 14 colleagues (2007) Mars Reconnaissance Orbiter's High Resolution Imaging Science Experiment (HiRISE). *J. Geophys. Res.*, *112*, 510.1029/2005JE002605.

McGuire, P. C., and 14 colleagues (2009) An improvement to the volcano-scan algorithm for atmospheric correction of CRISM and OMEGA spectral data. *Planet. Space Sci.*, *57*, 809-815 10.1016/j.pss.2009.03.007.

Milliken, R. E., and 11 colleagues (2008) Opaline silica in young deposits on Mars. *Geology*, *36*, 847-850, 10.1130/G24967A.1.

Moore, J. M and D. E. Wilhelms (2007) *Geologic Map of Part of Western Hellas Planitia*, Mars: U.S. Geological Survey Scientific Investigations Map 2953, scale 1:1,004,000.

Murchie, S., and 49 colleagues (2007) Compact Reconnaissance Imaging Spectrometer for Mars (CRISM) on Mars Reconnaissance Orbiter (MRO). *J. Geophys. Res.*, *112*, 510.1029/2006JE002682.

Mustard, J. F., B. L. Ehlmann, S. L. Murchie, F. Poulet, N. Mangold, J. W. Head, J.-P. Bibring, and L. H. Roach (2009), Composition, Morphology, and Stratigraphy of Noachian Crust around the Isidis basin, *J. Geophys. Res.*, *114*, 10.1029/2009JE003349.

Osterloo, M. M., V. E. Hamilton, J. L. Bandfield, T. D. Glotch, A. M. Baldridge, P. R. Christensen, L. L. Tornabene, and F. S. Anderson (2008) Chloride-Bearing Materials in the Southern Highlands of Mars. *Science*, *319*, 165110.1126/science.1150690.

Pelkey, S. M., and 11 colleagues (2007) CRISM multispectral summary products: Parameterizing mineral diversity on Mars from reflectance. *J. Geophys. Res.*, *112*, 810.1029/2006JE002831.

Poulet, F., J.-P. Bibring, J. F. Mustard, A. Gendrin, N. Mangold, Y. Langevin, R. E. Arvidson, B. Gondet, and C. Gomez (2005) Phyllosilicates on Mars and implications for early martian climate. *Nature*, *438*, 623-627 10.1038/nature04274.

Ramsey, M. S. and P. R. Christensen (1998) Mineral abundance determination: Quantitative deconvolution of thermal emission spectra. *J. Geophys. Res.*, *103*, 577-596 10.1029/97JB02784.

Rice, M.S., E.A. Cloutis, J.F. Bell III, D.L. Bish, B.H. Horgan, S.A. Mertzman, M.A. Craig, R.W. Renaut, B. Gautason, B. Mountain (2013) Reflectance Spectra Diversity of Silica-Rich Materials: Sensitivity to Environment and Implications for Detections on Mars, *Icarus*, *223*, 10.1016/j.icarus.2012.09.021.

Ruff, S. W. and P. R. Christensen (2007) Basaltic andesite, altered basalt, and a TES-based search for smectite clay minerals on Mars. *Geophys. Res. Lett., 34*, 1020410.1029/2007GL029602.

Ruff, S. W., and 10 colleagues (2011) Characteristics, distribution, origin, and significance of opaline silica observed by the Spirit rover in Gusev crater, Mars. *J. Geophys. Res.*, *116*, 010.1029/2010JE003767.

Smith, D. E., and 23 colleagues (2001) Mars Orbiter Laser Altimeter: Experiment summary after the first year of global mapping of Mars. *J. Geophys. Res.*, *106*, 23689-23722 10.1029/2000JE001364.

Smith, M. R., and J. L. Bandfield (2012) Geology of quartz and hydrated silica-bearing deposits near Antoniadi Crater, Mars. *J. Geophys. Res.*, *117*, 600710.1029/2011JE004038.

Smith, M. R., J. L. Bandfield, E. A. Cloutis, and M. S. Rice (2013) Hydrated Silica on Mars: Combined Analysis with Near-Infrared and Thermal-Infrared Spectroscopy. *Icarus*, in review.

Squyres, S. W., and 17 colleagues (2008) Detection of Silica-Rich Deposits on Mars. *Science*, 320, 106310.1126/science.1155429.

Sutter, B., J.B. Dalton, S.A. Ewing, R. Amundson, and C.P. McKay (2007), Terrestrial analogs for interpretation of infrared spectra from the Martian surface and subsurface: Sulfate, nitrate, carbonate, and phyllosilicate-bearing Atacama Desert soils, *J. Geophys. Res.*, *112*, 10.1029/2006JG000313.

Tosca, N. J. and A. H. Knoll (2009) Juvenile chemical sediments and the long term persistence of water at the surface of Mars. *Earth Planet. Sci. Lett.*, *286*, 379-386 10.1016/j.epsl.2009.07.004.

Tables

Table 1. List of CRISM images evaluated for this study. MSP prefix images are ~200 m/pixel multispectral survey data; FRT prefix images are acquired at full spectral and full spatial (~18 m/pixel) resolution; HRL and HRS prefix images are acquired at full spectral and half spatial (~36 m/pixel) resolution.

Multispectral Survey Images		Full Spectral Resolution	Discarded
MSP00002EE9_01	MSP000051F1_01	FRT0000847A_07	MSP0000688C_03
MSP000031F2_01	MSP000051F2_01	FRT00008FC6_07	MSP0000373F_01
MSP00003238_01	MSP00005280_05	FRT0000915D_07	MSP000037B0_01
MSP0000340F_01	MSP000053E8_01	FRT000091B7_07	MSP0000392C_01
MSP00003410_01	MSP000053E8_03	FRT00009317_07	MSP00005A43_07
MSP00003501_01	MSP00005447_05	FRT00009368_07	MSP0000688C_05
MSP00003502_01	MSP00005854_03	FRT000093C3_07	MSP0000698A_01
MSP00003541_01	MSP00005A73_03	FRT000094E6_07	MSP0000698A_03
MSP00003777_01	MSP00005C0E_01	FRT00009542_07	MSP00006AFA_03
MSP00003778_01	MSP00005C62_07	FRT000095A6_07	MSP00006AFA_05
MSP000038DC_01	MSP00005F66_07	FRT00009602_07	MSP00006D93_05
MSP000038DD_01	MSP00005FBA_03	FRT0000978A_07	MSP00007342_01
MSP00003ACF_01	MSP000060C0_01	FRT000097E4_07	MSP00007494_01
MSP00003C43_01	MSP000060C1_01	FRT00009A90_07	MSP00007494_03
MSP00003C44_01	MSP00006230_01	FRT00009AC1_07	MSP000074DA_03
MSP00003DD3_03	MSP000064DF_01	FRT00009BF8_07	MSP000079D6_01
MSP00003DD3_05	MSP000079D6_01	FRT00009D47_07	MSP00007E59_01
MSP00003F07_01	MSP00007BCC_07	FRT0000A158_07	MSP0000B407_01
MSP0000406E_07	MSP00008680_05	FRT0000A4B8_07	MSP0000B576_01
MSP000040C0_01	MSP00008720_03	FRT0000A4FF_07	MSP0000B812_01
MSP00004102_01	MSP0000882C_07	FRT0000A642_07	MSP0000BF79_01
MSP00004187_07	MSP000088D5_07	FRT0000A97C_07	MSP0000C208_01
MSP0000421D_01	MSP000088D6_01	FRT0000AAD1_07	MSP0000D699_01
MSP0000430A_05	MSP0000BBCE_01	FRT0000AB0F_07	MSP00011131_03
MSP0000430A_07	MSP0000BDAC_01	FRT0000B187_07	MSP00013914_01
MSP0000430A_07	MSP0000CBAF_01	FRT0000D3F3_07	MSP00014A40_01
MSP00004415_07	MSP000101D5_01	FRT000172E1_07	MSP000174A9_01
MSP00004416_01	MSP0001062B_01	FRT00017685_07	MSP00018687_01
MSP00004469_01	MSP00011131_05	FRT00017874_07	MSP000194F2_01
MSP0000450C_07	MSP000118CD_01	FRT0001C3C4_07	MSP00019B0A_01
MSP0000459F_01	MSP00013CE6_01	FRT0001C7C5_07	MSP0001A958_03
MSP00004992_01	MSP00014620_01	HRL0000A199_07	MSP0001A9AE_01
MSP00004992_03	MSP00014F05_01	HRL0000A1E8_07	MSP0001AB29_03
MSP00004ADD_01	MSP000154BF_01	HRL0000ADBF_07	MSP0001AB29_05
MSP00004ADD_03	MSP0001ACF1_07	HRL00011CC5_07	MSP0001AB73_05
MSP00004F17_01	MSP0001B89C_01	HRL00013366_07	MSP0001ACF1_05
MSP00004F17_03	MSP0001C63E_01	HRL0001637B_07	
MSP00004F7A_05		HRL000181A8_07	

	HRL0001BB51_07 HRS00009976_07 HRS0000A8C7_07 HRS0000B6A7_07 HRS00010EF1_07 HRS00013C7E_07 HRS00018C38_07

Table 2. Hydrated silica exposure locations (shown in Figure 2), areas, and elevations. Elevations are taken from the 16 pixel per degree MOLA gridded elevation map and may include interpolated elevation values.

Center E. Longitude	Center N. Latitude	Area (km^2)	Elevation (m)
47.82	-43.76	15.96	-5036
47.76	-43.69	19.54	-5378
48.33	-43.64	1.80	-5360
48.31	-43.55	0.88	-5374
48.12	-43.51	5.04	-5265
48.13	-43.47	0.40	-5300
48.14	-43.45	0.82	-5300
48.14	-43.42	0.04	-5313
48.10	-43.41	0.26	-5250
48.09	-43.40	0.18	-5250
48.12	-43.35	0.71	-5164
48.07	-43.34	0.35	-5164
48.42	-43.30	10.88	-5706
48.26	-42.85	26.66	-5362
48.22	-42.65	1.66	-5412
48.21	-42.53	4.81	-5665
48.18	-42.43	20.26	-5912
48.18	-42.12	5.44	-5751
48.09	-42.08	16.68	-5729
47.74	-41.96	1.84	-5074
47.79	-41.95	3.07	-5119
49.23	-41.93	9.61	-6363
47.65	-41.92	1.63	-5051
47.79	-41.90	4.04	-5125
48.04	-41.89	6.08	-5297
49.12	-41.86	18.39	-6242
48.10	-41.84	12.14	-5443
48.05	-41.66	38.91	-5399
48.20	-41.64	0.56	-5539
48.17	-41.59	9.05	-5513
48.10	-41.59	3.62	-5445

48.13	-41.54	0.33	-5505
48.06	-41.54	2.29	-5347
48.12	-41.50	3.07	-5443
48.06	-41.47	1.84	-5357
47.94	-41.19	4.37	-4988
49.03	-40.83	3.28	-6175
48.77	-38.81	19.16	-5683
48.93	-38.76	37.22	-5816
48.56	-38.12	8.85	-5592
48.64	-37.93	59.24	-5404
48.78	-37.73	4.05	-5584
49.24	-37.15	56.64	-5520
53.11	-33.72	0.91	-6572
53.06	-33.64	1.93	-6469
53.12	-33.60	4.12	-6377

Table 3. CRISM image lines and samples used for I/F ratio spectra in Hellas Basin shown in Figures 6 and 7. An average spectrum is calculated for the target and nearby null surfaces, and the two average spectra are divided to obtain the ratio spectra. Pixel locations are for unprojected CRISM data with north at the top of the image and X coordinates designate image column numbers and Y coordinates designate image row numbers.

CRISM Image ID	Numerator bounding pixels (target_region)	Denominator bounding pixels ("spectrally neutral" region)	Target Location
HRL00013366_07_IF181	X:155-170; Y:333-342	X:155-170; Y:391-402	48.12°E, 43.35°S
	X:138-147; Y:332-340	X:138-147; Y:372-380	48.14°E, 43.35°S
MSP00004ADD_01_IF214	X:43-51; Y:1494-1499	X:43-51; Y:1476-1482	47.83°E, 40.55°S
	X:28-36; Y:1503-1513	X:28-36; Y:1594-1604	47.88°E, 40.50°S
MSP00004415_07_IF214	X:49-51; Y:323-329	X:49-51; Y:271-277	49.00°E, 51.17°S
	X:43-45; Y:325-329	X:43-45; Y:264-268	49.03°E, 51.17°S

Figure Captions

Figure 1. THEMIS bands 6-4-2 decorrelation stretch mosaic (color) and THEMIS global daytime mosaic (grayscale; *Edwards et al.*, 2011), covering a region of numerous high-silica deposits. Magenta colors indicate regions containing high bulk silica deposits, cyan indicates basaltic compositions, and yellow/green colors indicate dust cover. The image is centered near 48.0°E, 42.2°S.

Figure 2. CRISM data coverage (shaded) and hydrated silica-bearing surface (white arrows/outlines) locations. The background image is Mars Orbiter Laser Altimeter (MOLA; *Smith et al.*, 2001) elevation (color) over the THEMIS daytime global infrared mosaic (*Edwards et al.*, 2011). The white box denotes the area shown in Figures 1 and 3.

Figure 3. CRISM hydrated silica 2.25 μm band depth index images with the THEMIS daytime global infrared mosaic used for shading. Only CRISM images with positive identifications of hydrated silica via manual inspection of individual spectra (orange and red areas; see Figure 2 for comparison) are shown. All images are stretched individually and index values are only comparable within each image. The image is centered near 48.0°E, 42.2°S and white boxes show areas covered by Figures 4 and 5. White circles indicate the locations of the images shown in Figure 8.

Figure 4. THEMIS bands 6-4-2 decorrelation stretch mosaic (from Figure 1; background in both images) with the CRISM hydrated silica 2.25 μm band depth index (left image overlay; CRISM image ID HRL00013366_07_IF181L_TRR3). Magenta colors in the THEMIS data (clearly visible in the northeast portion of the image) indicate the presence of high silica compositions.

Orange and red colors in the CRISM data indicate the presence of hydrated silica. The white arrows point to a location with hydrated silica deposits, but no corresponding detection of high bulk silica deposits in THEMIS data. The image is centered near 48.3°E, 43.3°S.

Figure 5. CRISM hydrated silica (top) and high Ca pyroxene (bottom) index images with CTX images used for shading. Hydrated silica bearing surfaces are commonly adjacent to basaltic sand surfaces (indicated by the presence of high Ca pyroxene) and dust devil tracks. The CRISM image ID is FRT0000B187_07_IF164L_TRR3, and CTX image ID's are P14_006687_1384_XI_41S311W and P13_006186_1384_XN_41S312W. The image is centered near 48.1°E, 41.6°S.

Figure 6. CRISM I/F ratio spectra of hydrated silica-bearing surfaces in western Hellas Basin compared with a laboratory opaline silica spectrum (scaled and offset; USGS spectral library ID TM8896). CRISM full spectral resolution data are from image ID HRL00013366_07_IF181L_TRR3 and the multispectral data are an average of CRISM image ID's MSP00004415_07_IF214L_TRR3 and MSP00004ADD_01_IF214L_TRR3 (Table 3). Shaded regions show the wavelength ranges used for the creation of the hydrated silica spectral index.

Figure 7. CRISM ratioed I/F spectra covering hydrated silica deposits in western Hellas Basin (red and blue; from Figure 6) compared with hydrated silica bearing surface spectra (offset) from Melas Chasma, Toro Crater, Noctis Labyrinthus, and Syrtis Major/Antoniadi Crater (from *Smith et al.*, 2013).

Figure 8. Surface textures associated with silica-bearing units in HiRISE (b-f) and CTX (a) images. Dashed lines, where present, denote boundaries of units with and without hydrated silica

signatures in CRISM data. Images (d), (e), and (f) are entirely within high-Si terrains. The compositional boundary in (b) coincides with a topographic step down to the high-Si terrain. The locations of each image are indicated in Figure 3.

Figure 9. Nighttime THEMIS temperature mosaic (color) overlaid on daytime THEMIS temperature mosaic (shading; *Edwards et al.*, 2011). Hydrated silica detections are shown by the white polygons. Cooler nighttime temperatures indicate lower thermal inertia surfaces. The white arrow show the location of a relatively low thermal inertia hydrated silica bearing surface with no corresponding high-Si detection using TIR data.

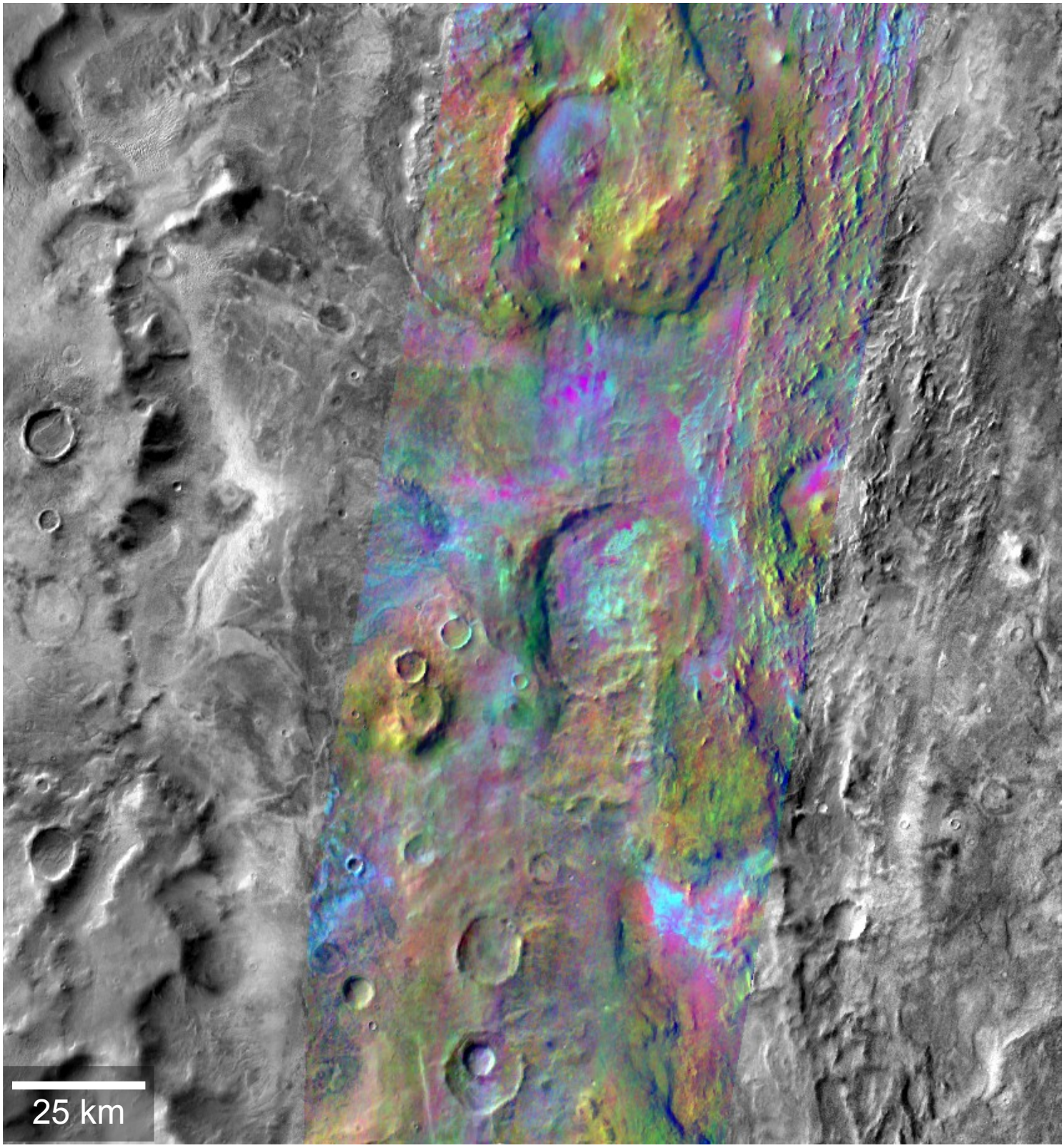

Figure 1. THEMIS bands 6-4-2 decorrelation stretch mosaic (color) and THEMIS global daytime mosaic (grayscale; *Edwards et al.*, 2011), covering a region of numerous high-silica deposits. Magenta colors indicate regions containing high bulk silica deposits, cyan indicates basaltic compositions, and yellow/green colors indicate dust cover. The image is centered near 48.0°E, 42.2°S.

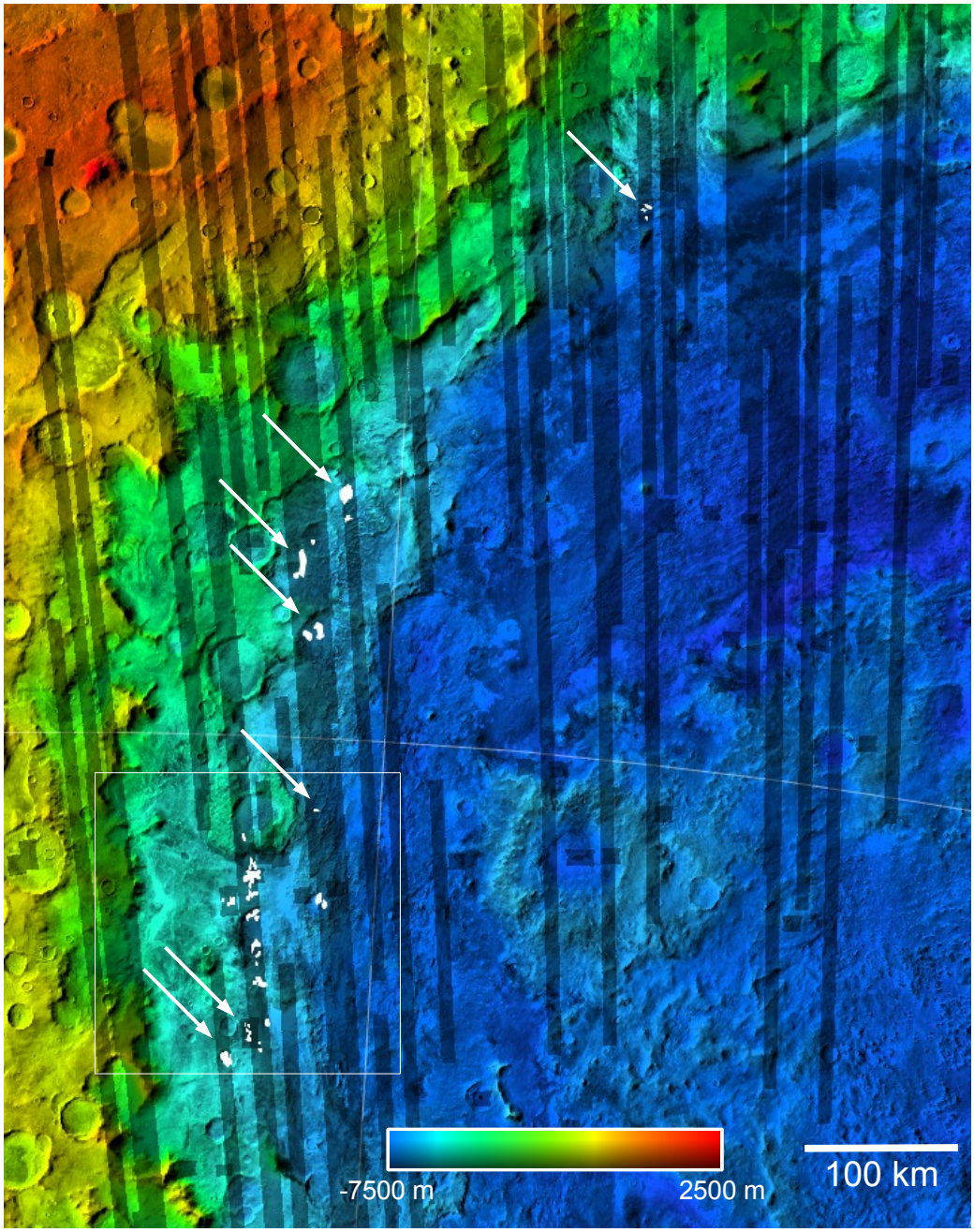

Figure 2. CRISM data coverage (shaded) and hydrated silica-bearing surface (white arrows/outlines) locations. The background image is Mars Orbiter Laser Altimeter (MOLA; *Smith et al.*, 2001) elevation (color) over the THEMIS daytime global infrared mosaic (*Edwards et al.*, 2011). The white box denotes the area shown in Figures 1 and 3.

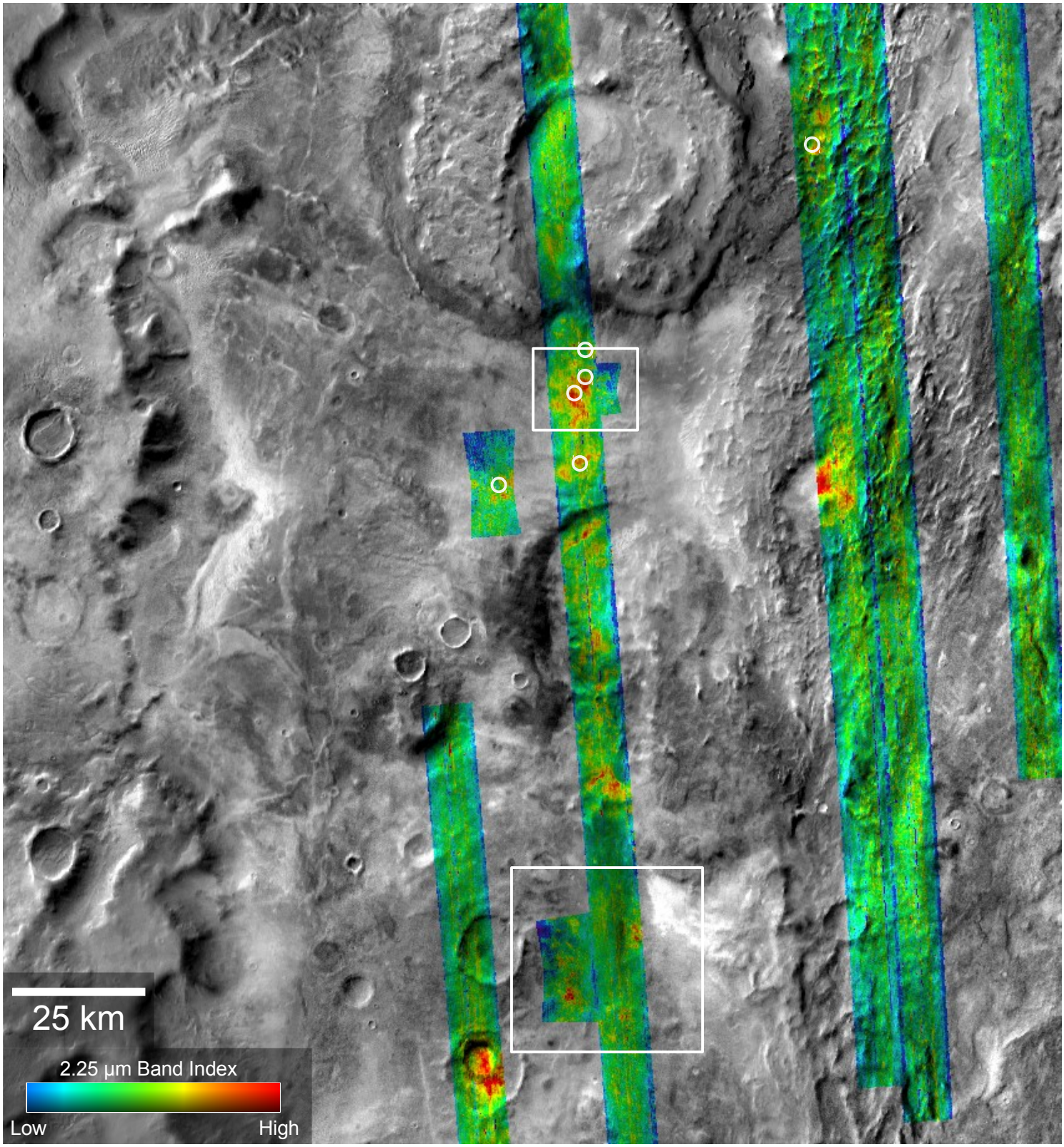

Figure 3. CRISM hydrated silica 2.25 µm band depth index images with the THEMIS daytime global infrared mosaic used for shading. Only CRISM images with positive identifications of hydrated silica via manual inspection of individual spectra (orange and red areas; see Figure 2 for comparison) are shown. All images are stretched individually and index values are only comparable within each image. The image is centered near 48.0°E, 42.2°S and white boxes show areas covered by Figures 4 and 5. White circles indicate the locations of the images shown in Figure 8.

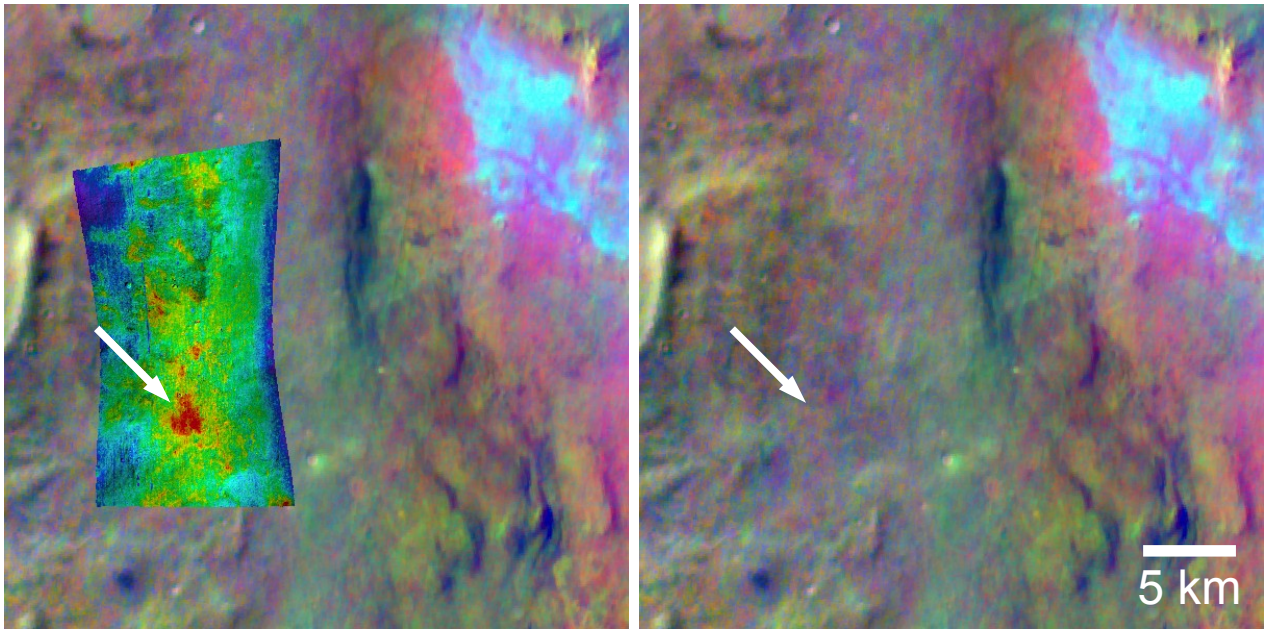

Figure 4. THEMIS bands 6-4-2 decorrelation stretch mosaic (from Figure 1; background in both images) with the CRISM hydrated silica 2.25 μm band depth index (left image overlay; CRISM image ID HRL00013366_07_IF181L_TRR3). Magenta colors in the THEMIS data (clearly visible in the northeast portion of the image) indicate the presence of high silica compositions. Orange and red colors in the CRISM data indicate the presence of hydrated silica. The white arrows point to a location with hydrated silica deposits, but no corresponding detection of high bulk silica deposits in THEMIS data. The image is centered near 48.3°E, 43.3°S.

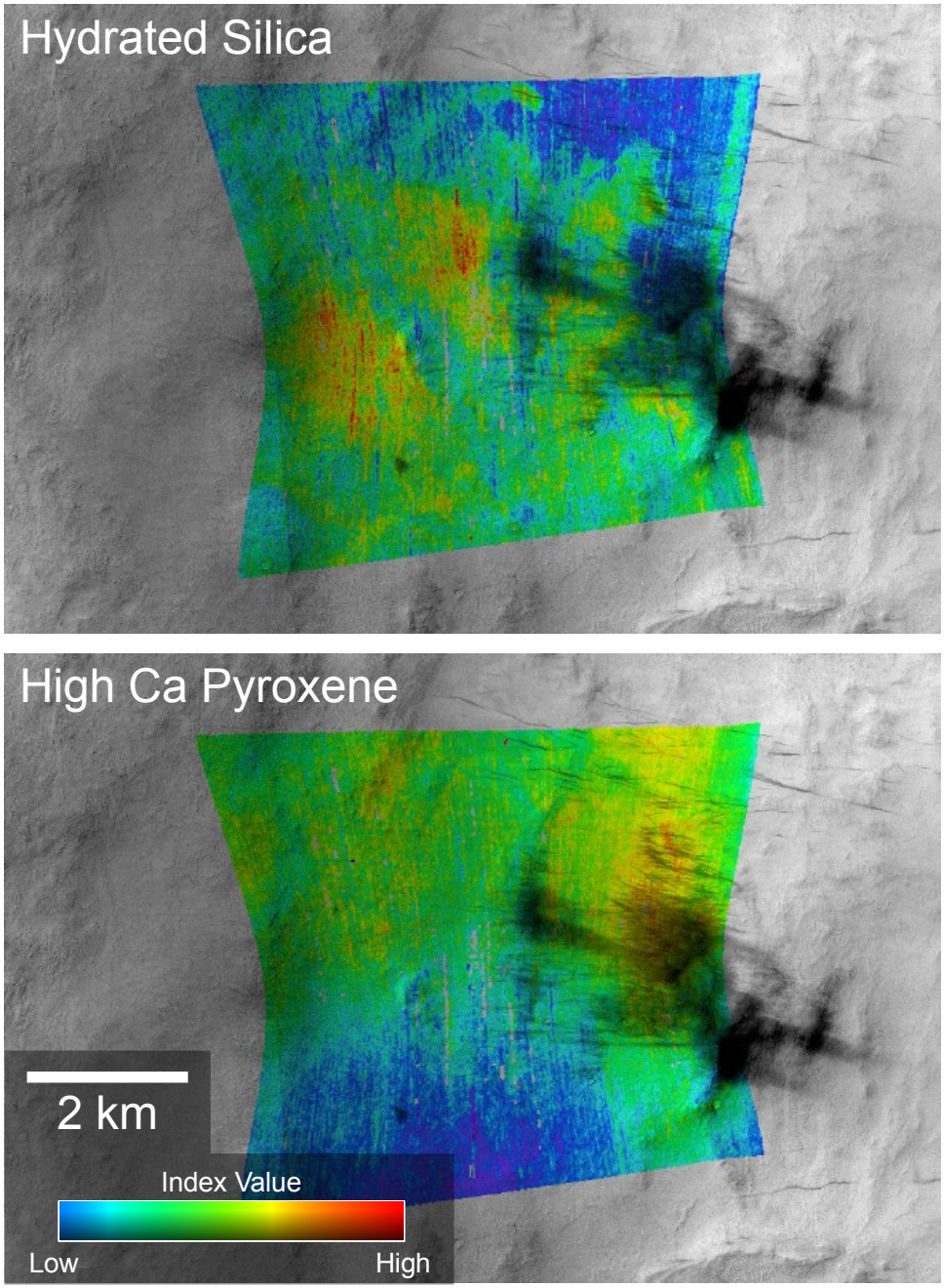

Figure 5. CRISM hydrated silica (top) and high Ca pyroxene (bottom) index images with CTX images used for shading. Hydrated silica bearing surfaces are commonly adjacent to basaltic sand surfaces (indicated by the presence of high Ca pyroxene) and dust devil tracks. The CRISM image ID is FRT0000B187_07_IF164L_TRR3, and CTX image ID's are P14_006687_1384_XI_41S311W and P13_006186_1384_XN_41S312W. The image is centered near 48.1°E, 41.6°S.

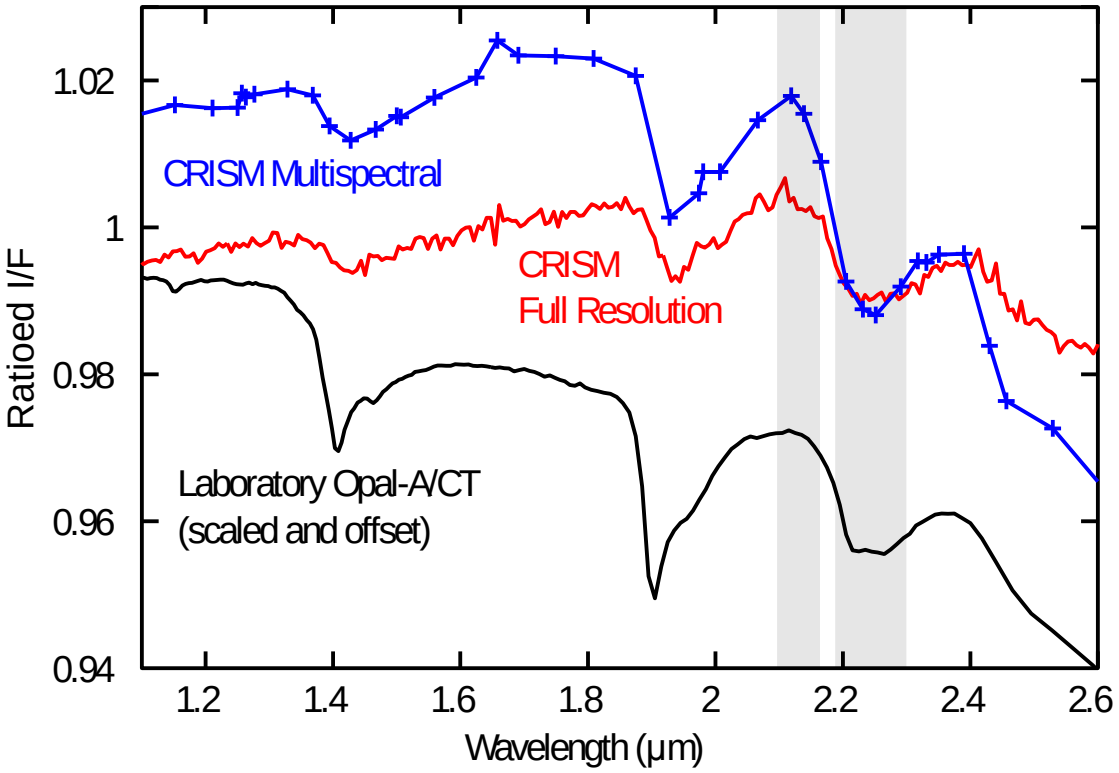

Figure 6. CRISM I/F ratio spectra of hydrated silica-bearing surfaces in western Hellas Basin compared with a laboratory opaline silica spectrum (scaled and offset; USGS spectral library ID TM8896). CRISM full spectral resolution data are from image ID HRL00013366_07_IF181L_TRR3 and the multispectral data are an average of CRISM image ID's MSP00004415_07_IF214L_TRR3 and MSP00004ADD_01_IF214L_TRR3 (Table 3). Shaded regions show the wavelength ranges used for the creation of the hydrated silica spectral index.

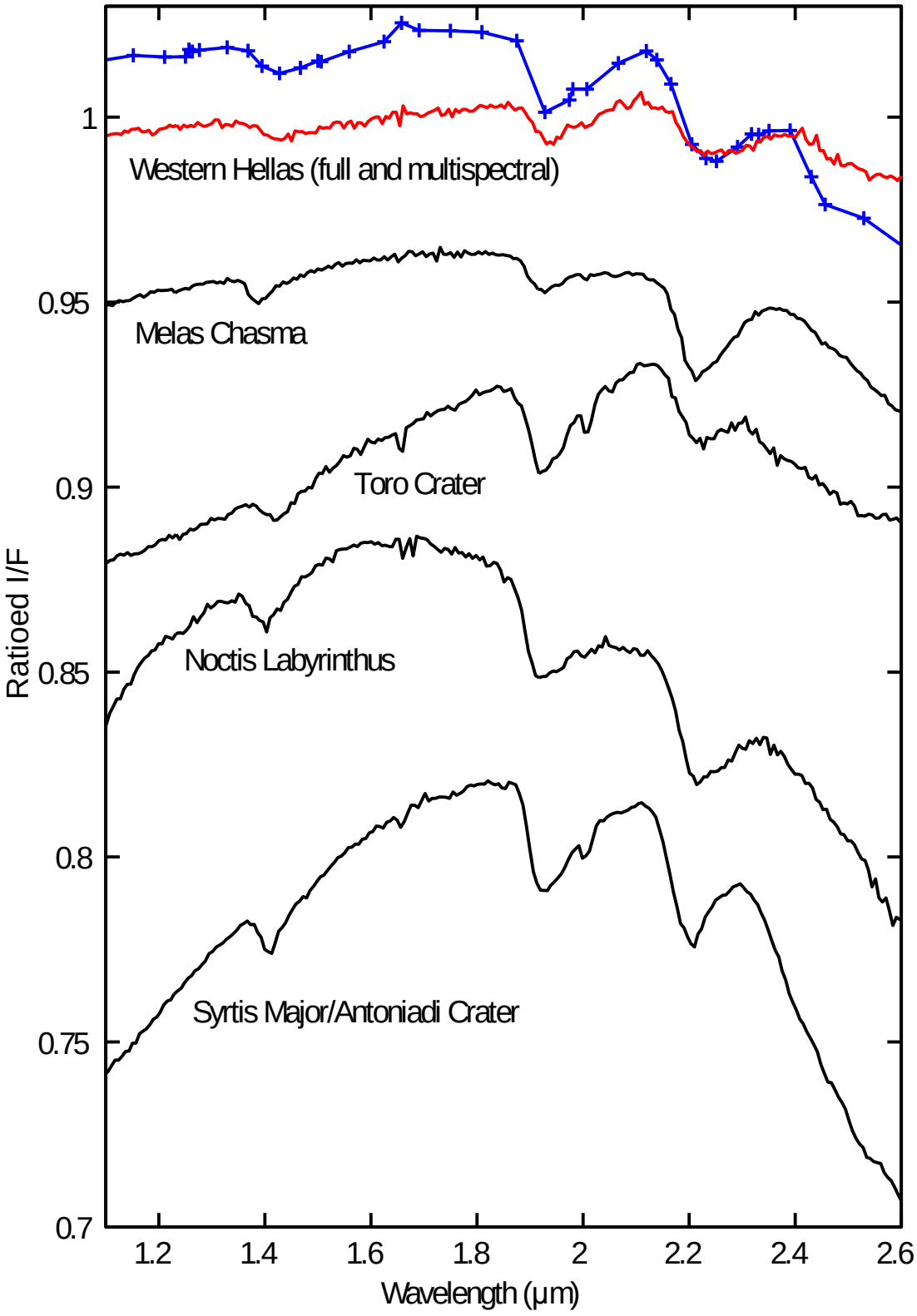

Figure 7. CRISM ratioed I/F spectra covering hydrated silica deposits in western Hellas Basin (red and blue; from Figure 6) compared with hydrated silica bearing surface spectra (offset) from Melas Chasma, Toro Crater, Noctis Labyrinthus, and Syrtis Major/Antoniadi Crater (from *Smith et al.*, 2013).

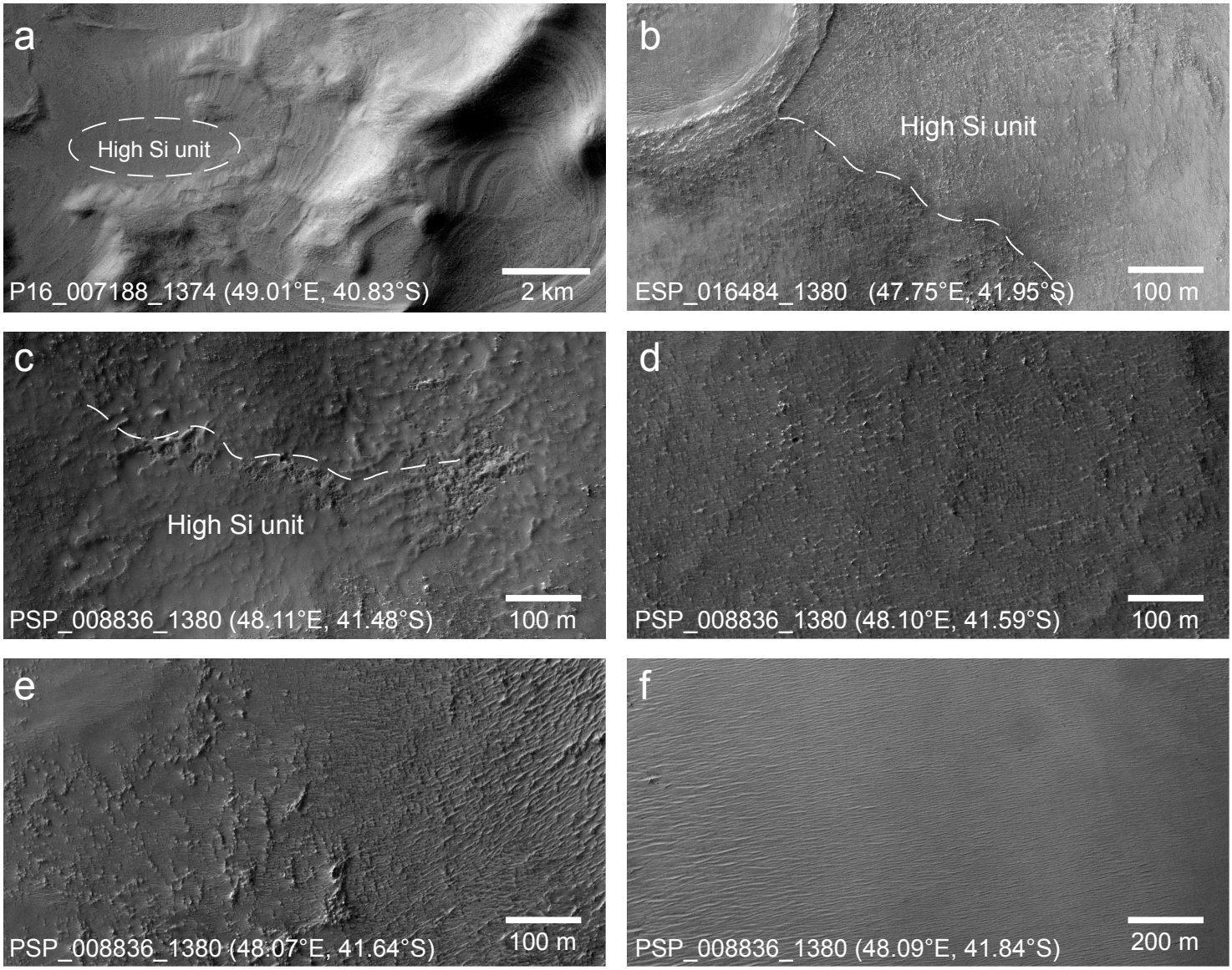

Figure 8. Surface textures associated with silica-bearing units in HiRISE (b-f) and CTX (a) images. Dashed lines, where present, denote boundaries of units with and without hydrated silica signatures in CRISM data. Images (d), (e), and (f) are entirely within high-Si terrains. The compositional boundary in (b) coincides with a topographic step down to the high-Si terrain. The locations of each image are indicated in Figure 3.

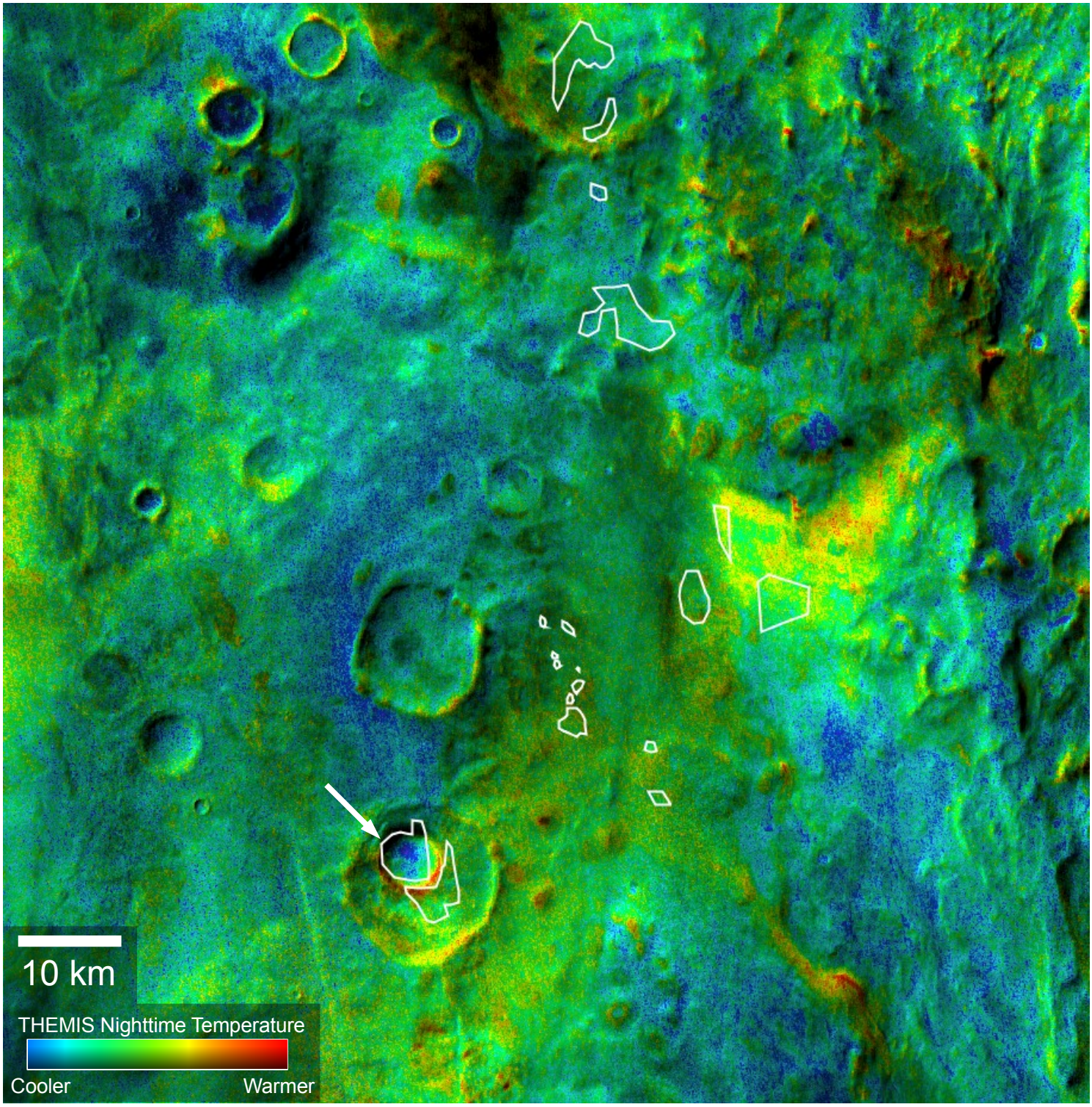

Figure 9. Nighttime THEMIS temperature mosaic (color) overlaid on daytime THEMIS temperature mosaic (shading; *Edwards et al.*, 2011). Hydrated silica detections are shown by the white polygons. Cooler nighttime temperatures indicate lower thermal inertia surfaces. The white arrow show the location of a relatively low thermal inertia hydrated silica bearing surface with no corresponding high-Si detection using TIR data.